First electrochemical Couette-Taylor reactor for studying the influence of transport phenomena on electrochemical kinetics

Florent Bouchon, Alain Bergel, Ahlem Filali, Théodore Bouchez, Yannick Fayolle

Florent Bouchon, Alain Bergel, Ahlem Filali, Théodore Bouchez, Yannick Fayolle. First electrochemical Couette-Taylor reactor for studying the influence of transport phenomena on electrochemical kinetics. Chemical Engineering Science, 2023, 281, pp.119103. 10.1016/j.ces.2023.119103 . hal-04295961

HAL Id: hal-04295961
https://hal.science/hal-04295961v1

Submitted on 20 Nov 2023

First electrochemical Couette-Taylor reactor for studying the influence of transport phenomena on electrochemical kinetics

Author names and affiliations

Florent Bouchon[1], Alain Bergel[2], Ahlem Filali[1], Théodore Bouchez[1] and Yannick Fayolle[1]

[1]Université Paris-Saclay, INRAE, PRocédés biOtechnologiques au Service de l'Environnement, 92761 Antony, France

[2] Laboratoire de Génie Chimique, Université de Toulouse, CNRS, INP, UPS, Toulouse, France

Corresponding author email yannick.fayolle@inrae.fr

Highlights

- The first electrochemical multi-electrodes Couette-Taylor reactor was developed
- Electrochemical responses to flow regimes were experimentally characterized
- Strictly turbulent and turbulent vortex flow gave similar electrochemical behavior
- Vortices and turbulence are the main driving forces of electrochemical reactions

Abstract

Electroactive biofilms are powerful catalysts of many electrochemical reactions of interest. Their development and electrochemical efficiency can be considerably dependent on the solution hydrodynamics. Unfortunately, analytical devices that are suited to the study of the effects of hydrodynamics on electroactive biofilms are still lacking. This study presents an electrochemical Couette-Taylor reactor (eCTR), which meets this objective. It integrated 20 large-sized electrodes individually addressed and exposed to the same hydrodynamics. Fluid dynamics was controlled by rotating the inner cylinder of the eCTR at speeds from 1 to 200 RPM. The device was characterized in abiotic condition using hexacyanoferrate (III/II) as model reactive species. The limiting currents (I_L) recorded with different concentrations of hexacyanoferrate and at different rotation speeds of the inner cylinder (ω) were used to calculate the Nernst diffusive layer thickness (δ_N), which ranged from 14.6 to 423 µm. Two hydrodynamic regimes were identified: the wavy vortex flow for ω from 1 to 10 RPM and the turbulent vortex flow for ω values higher than 15 RPM, which corresponded to the correlations $\delta_{N_{WVF}} \propto \omega^{-0.44}$ and $\delta_{N_{TVF}} \propto \omega^{-0.66}$, respectively. The second correlation confirmed the theoretical equation established by Gabe and Robinson for turbulent flow. In contrast, the wavy vortex flow was a specific regime, which cannot be approached by the laminar or turbulent hypothesis. Dimensionless correlations gave comparable results between eCTR and rotating cylinder electrodes under turbulent vortex flow and confirmed the specific behavior of the Couette-Taylor wavy vortex flow.

Keywords

Electrochemical layer thickness – Turbulent flow – Vortex flow – Hydrodynamics – Electroactive biofilm – Microbial electrochemical technology

Abbreviations

B	Constant parameter
b	Constant parameter
CTR	Couette-Taylor reactor
C_b	Concentration in the bulk (mol.m^{-3})
C_i	Concentration of the species *i* (mol.m^{-3})
C_s	Concentration on the electrode surface (mol.m^{-3})
CV	Cyclic Voltammetry
D_i	Diffusive coefficient of the species *i* (m^2.s^{-1})
D_{turb}	Apparent eddy viscosity (m^2.s^{-1})
eCTR	Electrochemical Couette-Taylor reactor
F	Faraday constant (C.mol^{-1})
I	Current (A)
I_L	Limiting current (A)
I_P	Current at the peak (A)
K	Constant from log regression
K_L	Convective mass transfer coefficient (m.s^{-1})
L	Characteristic length (m)
M	Width of the electrode (m)
n	Exponent of the shear rate
n_e	Number of electrons
N_i	Molar flux density of species *i* (mol.s^{-1}.m^{-2})
PVC	Polyvinyl Chloride
R^2	Coefficient of determination
r	Distance from the inner cylinder surface (m)
RCE	Rotating cylinder electrode

Re	Reynolds Number
R_i	Inner cylinder radius (m)
R_o	Outer cylinder radius (m)
RPM	Revolution Per Minutes
S	Electrode surface (m^2)
Sc	Schmidt number
SCE	Saturated Calomel Electrode
Sh	Sherwood number
TVF	Turbulent vortex flow
Ta	Taylor Number
Ta_c	Taylor critical value
U	Flow velocity ($m.s^{-1}$)
WVF	Wavy vortex flow
Greek letters	
α	Exponent of the angular velocity
Γ	Gamma function
$\dot{\gamma}$	Shear rate (s^{-1})
ΔV	Volt interval ($V.rot^{-1}$)
δ_I, δ_{II}	Diffusive layer thicknesses (m)
δ_N	Nernst diffusion layer thickness (m)
μ	Dynamic viscosity (Pa.s)
ν	Cinematic viscosity ($m^2.s^{-1}$)
σ	Scan rate ($V.s^{-1}$)
τ	Shear stress (Pa)
ω	Angular velocity ($rad.s^{-1}$)
ω_c	Critical velocity

Acknowledgements

The support of the French ANR for the PhD grant of Florent Bouchon in the framework of the project BIOTUBA (ANR-17-CE06-0015-01, 2018-2023) and of the DRRT Île-de-France for the financing of the reactor and the experiment are greatly appreciated. The STIM Company has participated to the design of the reactor. The partners of the project BIOTUBA (6TMIC and SIAAP) are also gratefully acknowledged.

1. Introduction

Electrochemical systems are used in many industrial applications [1–4] and microbial electrochemical technologies constitute an emerging field with multiple promising applications for power generation, resource recovery, chemicals production and sensing [5–12]. In such bio-electrochemical systems, multi-species biofilms play the role of the catalyst since they are able to exchange electrons with electrodes on which they develop [13,14]. The influence of electrolytes, electrode materials [15] or electrochemical parameters (applied current density and voltage or potential [16]) on the reaction associated with different physical parameters such as temperature, conductivity, pH or hydrodynamics are often studied to optimize those technologies [17,18]. However, the impact of fluid dynamics on electroactive biofilms was poorly investigated despite its major influence on their growth [19–21] and current density generation [22,23].

The experimental requirements to adequately study the influence of hydrodynamics on biofilm growth and long-term maturation are indeed numerous: (i) the electrodes size needs to be sufficient in order to allow recovery of biofilm samples in sufficient quantity for complete microbial characterization, (ii) the set-up should allow the continuous feeding and a homogeneous repartition of substrate all along the surface of the electrodes, (iii) multiple electrodes exposed to the same controlled hydrodynamics conditions need to be present to allow a sufficient level of replication of the measurements, which is mandatory considering the intrinsic experimental variability of biological systems under complex and variable media conditions during long term experiments.

Some experimental systems have actually been designed to study the impact of hydrodynamics on biofilms in continuous flow such as flow cells [22–25]. They were used to study precise hydrodynamics in microfluidic channels where the shear stress is induced by the flow rate [26]. In the specific case of electroactive biofilms, they could be developed on small electrodes implemented in the cell (generally up to 1 cm²) allowing having the same applied shear stress on the whole surface. Experiments were run at daily or weekly scale [27]. They were often couple with non-invasive imaging technologies such as microscopy to analyze biofilm structural parameters overtime (thickness, density, porosity, etc. [28,29]). Thus they allow a great characterization of the biofilm but some limitation appeared considering their small size, which does not allow biofilm sampling overtime or having replicates under the identical operating conditions.

Other systems were employed for the study of fluid dynamics impact on electrochemical technologies [30,31]. The most well-known systems are the rotating disk electrodes described by

Levich [32]. Electrochemical reactions take place on the surface of a small rotating electrode (lower than 1 cm²) and the current is expressed as a function of the rotation speed. Nonetheless, only a few studies have shown biofilm development on rotating disk electrodes [33]. Some variants such as the rotating cylinder electrodes (RCE) implement a cylinder-electrode immerged in the electrolyte as described by Eisenberg *et al.* [34]. They were adapted to larger surfaces of electrodes (> 10 cm²) [35–37] but RCE have mainly been described considering abiotic mass transfer and not for the study of electroactive biofilms [34].

Couette-Taylor reactors (CTR) have a perfectly described hydrodynamic profile and have been often used for the study of biofilm development for scale-up purposes [38–40]. They are composed of two concentric cylinders, with a rotating inner cylinder and a fixed outer cylinder (respectively characterized by the radii R_i and R_o). The main differences of CTR in comparison to RCE are the various hydrodynamic conditions from well-known Couette flow to 3D typical vortices flows or turbulent flows induced by the specific influence of the stationary outer wall [40]. CTR may apply a higher range in terms of shear stress induced on the surface of the inner cylinder classically from 0.1 to 10 Pa in aqueous media [38,41], compared to rotating electrodes under high shear stress and turbulent flows [42,43]. In previous studies, CTR were used to study hydrodynamics influence on physical biofilm properties and allowed characterization and sampling of biofilm along time (density, thickness, porosity, etc.) [44–47]. However, no adaptation to such reactor was made for the integration of electrodes in the set-up in order to study electroactive biofilms.

In fact, some work has been done to couple electrochemistry analysis with CTR hydrodynamics. Sobolík *et al.* [48] introduced a single three-segment electrodiffusion probe in two different CTR with radius ratio R_i/R_o of 0.84 and 0.7 respectively. They have thus characterized components of the shear rate on the outer wall under wavy vortex flows. Berrich *et al.* [49] have characterized a Couette-Taylor-Poiseuille flows (for vortex and wavy vortex regimes) in an larger CTR (radius ratio of 0.86) implementing 39 microelectrodes distributed along the circumference and a vertical segment of the outer cylinder. Legrand *et al.* [50] have performed one of the first characterization of the mass transfer occurring in Couette-Taylor-Poiseuille flows for wavy vortex flows thanks to electrochemical measurement in CTR (radius ratio of 0.78). Their reactor integrated a 3 segments inner cylinder (composed of the cathode framed in the anode). Nevertheless, those methodologies were developed to study hydrodynamics and mass transfer in CTR and were not dealing with electrodes allowing biofilm development: (i) microelectrodes for Sobolik *et al.* [48] and Berrich *et al.* [49] and (ii) nickel-cathode covered by platinum and gold for Legrand *et al.* [50] which are not the preferred materials for biofilm growth [51].

In this study, the first electrochemical CTR is presented. The main specificities of this reactor are (i) 20 graphite electrodes included in the inner rotating cylinder allowing to have replicates in exactly the same hydrodynamic conditions, with a (ii) large surface (20 cm²) under uniform well-known hydrodynamics, allowing (iii) spontaneous biofilm development in real conditions including complex effluents but with (iv) independent electrical connections for each electrode.

The reactor is characterized experimentally for various operating conditions under wavy and turbulent vortex flows without biofilm development considering (i) electrochemical parameters, (ii) small ascendant flow rate, (iii) concentration of the electroactive species and (iv) effect of the rotation speed of the inner cylinder. Then, the results are interpreted in light of previous theoretical analysis of Gabe & Robinson [52,53], which describes the relation between current intensity and the flow velocity in laminar [52] and turbulent flow regimes [53]. Finally the results are compared to previous studies on different hydrodynamic regimes (Eisenberg *et al.* [34] and Legrand *et al.* [50]) and the potential application of the electrochemical CTR for future studies is discussed.

2. Materials and Methods

2.1. Electrochemical Couette-Taylor Reactor (eCTR)

The Couette-Taylor reactor was composed of two coaxial cylinders of 25 cm height (Figure 1A). The rotating inner cylinder, of 7 cm radius, includes 20 graphite-plate (Sigraform HLM, Graphitech) working electrodes inlaid in the PVC cylindrical core. Each working electrode had a surface of 20×1 cm² and was immersed by 18 cm. The active projected area of each working electrode was thus 18 cm^2. Each electrode was individually connected to the external electrical circuit thanks to a rotating collector (SVTS C 03-S-A-00/18). The central axis of the inner cylinder was mechanically connected to a motor (APM-SA01) by means of a speed reducer (PLGE12/1 i=9) and could thus be rotated at speeds from 1 to 200 RPM. The non-mobile outer cylinder, made of stainless steel (316L) of 10 cm radius, was used as the auxiliary electrode. A calomel reference electrode (SCE, BioLogic, +0.244 V/SHE) was positioned between the two cylinders about 1.5 cm from the outer cylinder. The lid and the base of the reactor as made from PVC. The reactor was set in a solution circulation loop equipped with a peristaltic pump (Gilson), which provided a flow rate of 700 mL.h^{-1} (axial solution velocity in the reactor of 4.38 cm/h). The flow inlet was at the reactor bottom and the outlet ensured a water level of 20 cm, i.e.

a volume of solution in the reactor of 3.6 L. All experiments were conducted in a 25°C temperature-regulated room.

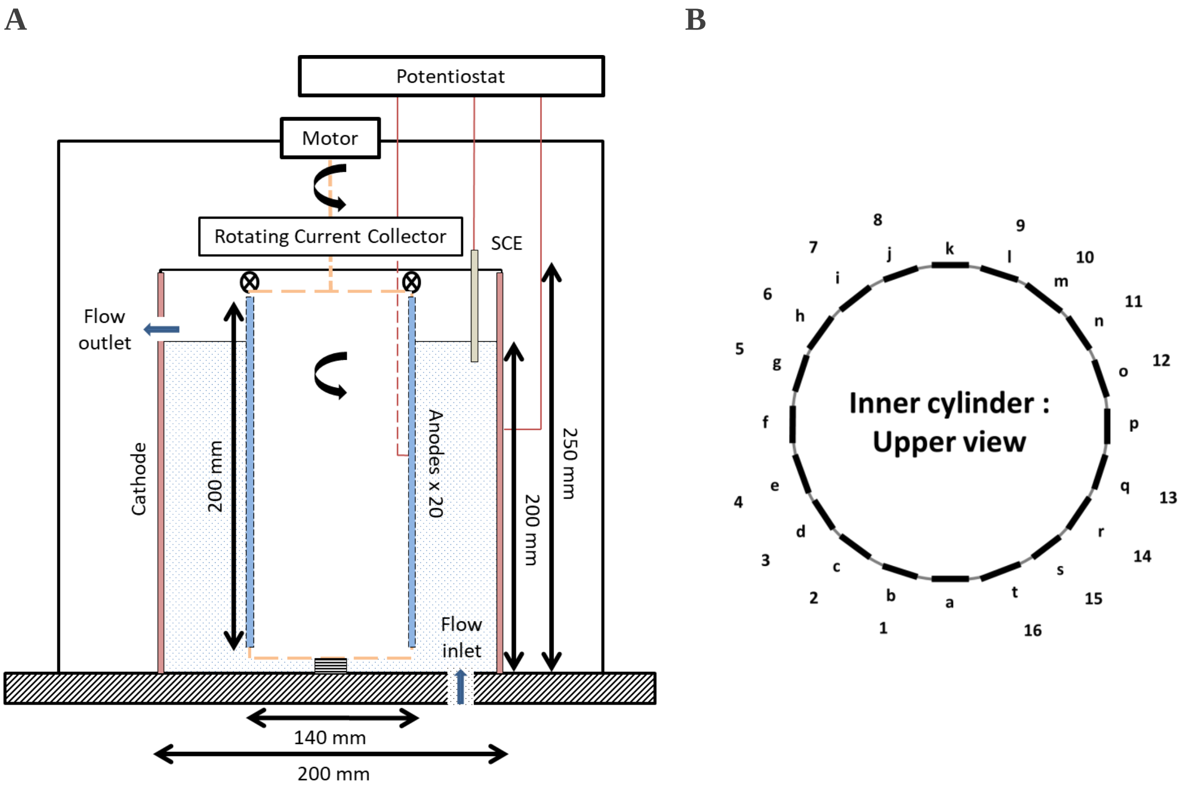

Figure1: A) Diagram of electrochemical Couette-Taylor reactor and B) visualization in top view of the inner cylinder with position of the electrodes.

Up to 16 working electrodes could be individually addressed with a multi-channel potentiostat (VMP-3, Biologic). Two Nstat boxes (Biologic) were used to integrate each working electrode in a 3-electrode set-up with the single SCE as the reference electrode and the fixed outer cylinder as the auxiliary electrode. Each working electrode was identified by a letter from *a* to *t* (Figure 1B). Electrodes *b* to *j*, excluding electrode *f*, were connected via an Nstat to the tracks 1 to 8 of the potentiostat. The other group, from *l* to *t*, excluding electrode *p*, were connected to the tracks 9 to 16 via the other Nstat. Four electrodes (*a*, *f*, *k*, and *p*) were not electrochemically connected. They will serve as controls in future experiments that will be devoted to the study of microbial electroactive biofilms.

Cyclic Voltammetries (CV) were performed with scan rates from 1 to 100 mV.s^{-1} in the range of -0.35 to +0.65 V/SCE. Three successive cycles were systematically performed. The first cycle was sometimes slightly different from the second and third cycles, which were always identical. All the data reported in the present study were extracted from the second CV cycles.

2.2.Solutions

Solutions of equimolar potassium hexacyanoferrate (III) and hexacyanoferrate (II) ($Fe(CN)_6^{3-}$ /$Fe(CN)_6^{4-}$) were used at different concentrations, from 1 mM to 20 mM. Hexacyanoferrate was chosen as model electroactive species because it ensured fast electron transfer with carbon-based electrodes. The solution was supplemented with mono-basic and di-basic phosphate (NaH_2PO_4 and Na_2HPO_4) 100 mM. The potassium, sodium and phosphate ions provided thus the main part of ion migration in solution and the migration contribution can be neglected in the mass transport of hexacyanoferrate.

The diffusive coefficient of hexacyanoferrate (II) is given by the relation of Stokes-Einstein at 25°C and is equal to 5.09×10^{-10} $m^2.s^{-1}$.

3. Theoretical description

3.1.Hydrodynamic modelling

The flow regimes in CTR are described according to the dimensionless Taylor number (Ta) [54] which characterizes the centrifugal force applied to the liquid in relation to the viscous force the liquid opposes to the motion:

$$Ta\ =\frac{\omega\sqrt{R_i(R_o-R_i)^3}}{\nu} \tag{1}$$

where ω is the angular velocity (rad.s^{-1}), R_i and R_o the radii of the inner and the outer cylinder (m) and ν the cinematic viscosity ($m^2.s^{-1}$). The Ta number can be considered as a form of the Reynolds number Re adapted to the specific geometry of the CTR:

$$Ta\ = Re\sqrt{\frac{(R_0-R_i)}{R_i}} \tag{2}$$

where $Re=\frac{\omega R_i(R_0-R_i)}{\nu}$

The Ta number allows describing the different flow regimes according to the value it takes regarding a critical value Ta_c [55,56] :

$$Ta_c=\ 20.65\frac{R_o\left(1+\frac{R_i}{R_o}\right)^2}{R_i\sqrt{\left(1-\frac{R_i}{R_o}\right)\left(3+\frac{R_i}{R_o}\right)}}\sqrt{\frac{R_o-R_i}{R_i}} \tag{3}$$

For the eCTR designed in this study, $R_o=0.10$ m, $R_i=0.07$ m (corresponding to a radius ratio of 0.7) and $\nu=10^{-6}\ m^2.s^{-1}$ give Ta_c = 53.0 [-], which corresponds to the critical velocity value ω_c of 0.039 rad.s^{-1} (0.37 RPM). The correspondences between Ta values, the flow regimes and ω values are given in table 1. The reactor was operated with different values of ω from 1 to 200

RPM (respectively 1, 3, 5, 6.5, 8, 10, 15, 25, 50, 100, 150 and 200). This choice was made considering the capacity of the motor to ensure stable rotating velocity values and in order to cover the largest velocities ranges and associated flow regimes (from vortex to turbulent vortex regimes, according to Table 1).

The Sherwood number (*Sh*) characterizes the ratio of the convective and diffusive mass transport [57]:

$$Sh = \frac{K_L L}{D_i} \tag{4}$$

where K_L is the convective mass transfer coefficient (m.s^{-1}), $L = R_o - R_i$ the characteristic length in Couette-Taylor reactors, which is the gap between the inner and the outer cylinder (m) and D_i is the effective diffusive coefficient (m^2.s^{-1}).

The Sherwood number is generally expressed as a function of the Reynolds number (*Re*) and the Schmidt (*Sc*) number defined by $Sc = \nu / D_i$, according to experimental correlations.

Table 1: Couette-Taylor flow regimes, and corresponding Ta, rotation speed equivalent boundaries and shear stress values

Regime	*Ta* range	*Ta* values	*ω* (rad.s^{-1})	*ω* (RPM)	*τ* (mPa)
Couette Laminar	$Ta < Ta_c$	$Ta < 53$	$\omega < 0.039$	$\omega < 0.37$	$\tau < 0.039$
Vortex	$Ta_c < Ta < 1.27\, Ta_c$	$53 < Ta < 67$	$0.039 < \omega < 0.049$	$0.37 < \omega < 0.47$	$0.039 < \tau < 0.049$
Wavy Vortex	$1.27\, Ta_c < Ta < 40\, Ta_c$	$67 < Ta < 2120$	$0.049 < \omega < 1.55$	$0.47 < \omega < 14.8$	$0.049 < \tau < 27$
Turbulent Vortex	$40\, Ta_c < Ta < 700\, Ta_c$	$2120 < Ta < 37100$	$1.55 < \omega < 27$	$14.8 < \omega < 258$	$27 < \tau < 4300$
Turbulent	$Ta > 700\, Ta_c$	$Ta > 37100$	$\omega > 27$	$\omega > 258$	$\tau > 4300$

Under laminar flow conditions (Table 1), the velocity of a Couette-Taylor flow *U* (m.s^{-1}) only depends on the distance from inner cylinder *r* and is given by [43]:

$$U = \omega R_i^2 \frac{\left(\frac{1}{r} - \frac{r}{R_o^2}\right)}{\left(1 - \frac{R_i^2}{R_o^2}\right)} \tag{5}$$

The fluid shear stress is a function of the fluid velocity and the dynamic viscosity according to:

$$\tau = \mu \, div \, U \tag{6}$$

where τ is the shear stress applied on the cylinder wall (Pa), μ is the dynamic viscosity (Pa.s) and U the fluid velocity (m.s^{-1}).

Under laminar flow conditions, the velocity profile (equation 5) used in equation 6 gives the shear stress on the surface of the inner cylinder ($r = R_i$):

$$\tau = \mu\omega \tag{7}$$

Former work in the literature [54] describes the expression of the shear forces applied to the rotating inner wall as function of the Reynolds number under Couette-Taylor flows:

$$\tau = 2.13 \frac{(R_i/R_o)^{3/2}}{[(R_o-R_i)/R_o]^{7/4}} Re^{1.445} \frac{\rho v^2}{2\pi R_i^2} \qquad \text{For } Re > 800 \ (\omega > 3.65 \text{ RPM}) \tag{8}$$

$$\tau = 0.113 \frac{(R_i/R_o)^{3/2}}{[(R_o-R_i)/R_o]^{7/4}} Re^{1.764} \frac{\rho v^2}{2\pi R_i^2} \qquad \text{For } Re > 10^4 \ (\omega > 47 \text{ RPM}) \tag{9}$$

where ρ is the fluid density (kg.m^{-3}).

3.2.Relation between fluid velocity and current

The molar flux density of a solute *i* is the sum of 3 components due to diffusion, migration and convection [57]. Generally, solutions used in electroanalytical studies contain a supporting salt and/or a charged buffer compound at high concentration, as it was the case here (NaH_2PO_4 and Na_2HPO_4), so that the migration flux can be neglected for solutes. Furthermore, for low concentration of solutes, the diffusion flux can be expressed according to the Fick's law. So the molar flux density ($\overrightarrow{N_i}$, mol.s^{-1}.m^{-2}) of a solute *i* at low concentration can be written as:

$$\overrightarrow{N_i} = -D_i \overrightarrow{grad} C_i + C_i \vec{U} \tag{10}$$

where D_i is the effective diffusive coefficient (m^2.s^{-1}), C_i is the concentration (mol.m^{-3}) and $\vec{U}$ is the fluid velocity (m.s^{-1}).

At steady state and in the absence of reaction in solution, the differential mass balance equation for the species *i* is:

$$div \, \overrightarrow{N_i} = 0 \tag{11}$$

and leads to:

$$div\left(-D_i\overrightarrow{grad}C_i + C_i\vec{U}\right) = 0 \quad (12)$$

At steady state, the current $\vec{I}$ (A) is proportional to the molar flux of the electroactive species at the electrode surface. When only one electroactive species *i* is oxidized at the electrode surface, as it was the case here, the current is expressed as:

$$\vec{I} = n_e FS\vec{N}_{i|electrode} \quad (13)$$

where n_e is the number of electrons produced per molecule of electroactive species, F is the Faraday constant (96 485 C.mol^{-1}) and S is the surface area of the electrode (m^2).

3.2.1. Nernst model

The Nernst model divides the solution space into two zones: a stagnant boundary layer against the electrode surface and a perfectly stirred bulk beyond the stagnant layer (Figure 2A). The concentration is uniformly equal to C_b in the bulk. Equation 12 can thus be solved very simply in the stagnant layer, in which $U = 0$, and, combined with equation 13, gives:

$$I = n_e\, D_i\, F\, S \frac{C_b - C_s}{\delta_N} \quad (14)$$

where C_b and C_s are the concentrations of the electroactive species in the bulk and at the electrode surface, respectively (mol.m^{-3}) and δ_N is the thickness of the Nernst layer (m). The limiting current I_L is defined as the maximal value of the current that can be reached when only the diffusion transport is rate-limiting, i.e. when the electrochemical reaction is so fast in relation to mass transport that the electroactive species reacts at the electrode surface as soon as it reaches it, resulting in $C_s = 0$. According to equation 14, in the framework of the Nernst's model, the limiting current is:

$$I_L = n_e\, F\, S \frac{D_i}{\delta_N} C_b \quad (15)$$

Nernst model allows expressing the convective mass transfer coefficient K_L as a function of δ_N according to:

$$K_L = \frac{D_i}{\delta_N} \quad (16)$$

In a CTR, the Nernst layer thickness δ_N depends on the rotation speed. More sophisticated models are needed to obtain a theoretical relationship between the layer thickness and the rotation speed.

3.2.2. Gabe and Robinson model for laminar flow

Under laminar flow conditions, Gabe & Robinson [52] considered that the annulus geometry of a CTR can be approached as a straight channel for a small length M ($M \ll 2\pi R_i$) parallel to the flow. They defined the x- and y-axes as parallel and perpendicular to the channel length, respectively. They assumed that mass transport was ensured only by the fluid flow along the x-axis and only by diffusion along the y-axis, so that equation 12 becomes:

$$-D_i \frac{d^2 C_i}{dy^2} + U \frac{dC_i}{dx} = 0 \tag{17}$$

in which the fluid velocity *U* is given by equation 5. They used a change of variable to transform the equation in one dimension. Then, they obtained an expression for the current:

$$I \ = \frac{3^{4/3}}{2\Gamma(1/3)} n_e F S D_i^{2/3} (c_b - c_s) M^{-1/3} \left(\frac{1+{R_i}^2/{R_o}^2}{1-{R_i}^2/{R_o}^2}\right)^{1/3} \ \omega^{1/3} \tag{18}$$

where *Γ* is the Gamma function and *M* the width of the electrode (m). Under laminar flow conditions, the limiting current according to the Gabe & Robinson [52] approach is consequently:

$$I_L \ = \frac{3^{4/3}}{2\Gamma(1/3)} n_e F S D_i^{2/3} \ c_b \ M^{-1/3} \left(\frac{1+{R_i}^2/{R_o}^2}{1-{R_i}^2/{R_o}^2}\right)^{1/3} \ \omega^{1/3} \tag{19}$$

Comparing with the Nernst expression (equation 15) allows extracting an expression of an equivalent Nernst layer in laminar condition ($\delta_{N-Gabe\ lam}$):

$$\delta_{N-Gabe\ lam} \ = \frac{2\Gamma(1/3)}{3^{4/3}} D_i^{1/3} \ M^{1/3} \left(\frac{1+{R_i}^2/{R_o}^2}{1-{R_i}^2/{R_o}^2}\right)^{-1/3} \ \omega^{-1/3} \tag{20}$$

Sherwood number could then be expressed according to equation 16 and 20 as:

$$Sh = Re^{1/3} Sc^{1/3} \frac{3^{4/3}}{2\Gamma(1/3)} \left[\frac{(R_i - R_i)^2 (1+{R_i}^2/{R_o}^2)}{R_i M (1-{R_i}^2/{R_o}^2)}\right]^{1/3} \tag{21}$$

3.2.3. Gabe and Robinson model for turbulent flow

Under turbulent flow conditions, Gabe & Robinson [53] used the 3-zone model from Prandtl-von Karman (Figure 2B), in which the layer next to the electrode surface (zone I) is considered as a Nernst boundary layer and the zone III, the furthest from the electrode surface, is considered in fully developed turbulence. Considering a planar geometry, the Nernst approach applied to zone I gives:

$$I = n_e F S D_i \frac{C_I - C_s}{r} \tag{22}$$

where C_I is the concentration (mol.m^{-3}) of the electroactive species in zone I at the distance r (m) from the electrode surface. This equation gives the concentration profile in zone I:

$$C_I = C_s + \frac{I\,r}{n_e F S D_i} \tag{23}$$

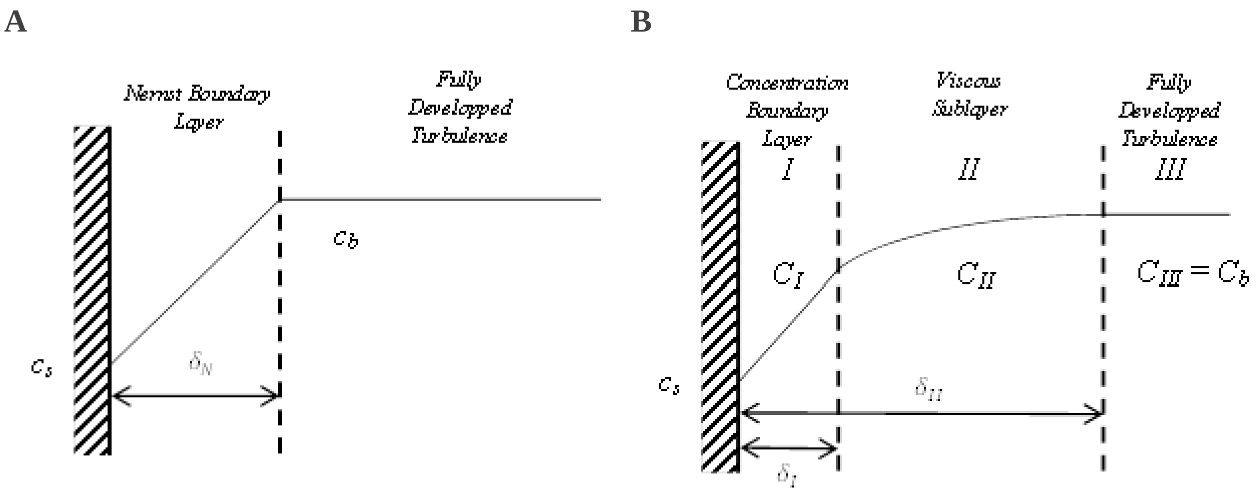

Figure 2: Models of mass transport near the electrode surface. The electrode is the surface of the inner cylinder of the CTR. A) Nernst model. B) 3-zone model according to Prandtl-von Karman (from [53]).

In the intermediary viscous layer (zone II), Gabe & Robinson [53] assumed that mass transport is achieved by convection and eddy diffusion, so that equation 10 is transformed to:

$$\text{div}\,(-D_{turb}\,\overrightarrow{grad}C_i + C_i\vec{U}) = 0 \tag{24}$$

where D_{turb} (m^2.s^{-1}) is the apparent eddy viscosity and varies with the flow velocity. Assuming that U is constant in zone II and equal to ωR_i, D_{turb} could be expressed as:

$$D_{turb} = \frac{b r^3 \omega^2 R_i}{\nu} \tag{25}$$

where r is distance from the electrode surface (m), ν the cinematic viscosity (m^2.s^{-1}) and b a constant. Solving equations 23 gives the concentration profile in zone II:

$$C_{II} = C_b + \frac{I\nu}{2 n_e F S b \omega^2 R_i}\left(\frac{1}{{\delta_{II}}^2} - \frac{1}{r^2}\right) \tag{26}$$

where δ_{II} is the thickness of the zone II. At the interface between the zones I and II, i.e. at $r = \delta_I$, the equations 23 and 26 must give the same concentration value. Writing this gives a relationship between δ_I and δ_{II} and considering that $\frac{{\delta_I}^3}{{\delta_{II}}^2} \ll \delta_I$ leads to the expression of the current as:

$$I = n_e F S \left(\frac{BR_i}{\nu}\right)^{1/3} (\omega D_i)^{2/3} (C_b - C_s) \qquad (27)$$

where $B = \left(\frac{2}{3}\right)^3 b$. The limiting current I_L is consequently:

$$I_L = n_e F S \left(\frac{BR_i}{\nu}\right)^{1/3} {D_i}^{2/3} C_b \ \omega^{2/3} \qquad (28)$$

Comparing with the Nernst expression (equation 15) allows extracting an equivalent Nernst layer in turbulent condition ($\delta_{N-Gabe\ turb}$) as:

$$\delta_{N-Gabe\ turb} = \left(\frac{D_i \nu}{BR_i}\right)^{1/3} \ \omega^{-2/3} \qquad (29)$$

which gives the Sherwood number according to equation 16 and 29:

$$Sh = Re^{2/3} Sc^{1/3} \left(\frac{B(R_o - R_i)}{R_i}\right)^{1/3} \qquad (30)$$

4. Results

4.1. Preliminary characterization of the reactor

4.1.1. Influence of the inlet flow without rotation

The eCTR was equipped with electrodes of large surface areas, which covered the entire inner (working electrode) and outer (auxiliary electrode) cylinders. The electrochemical reactions can consequently drastically affect the concentration of the reactive species, so that the stationary state may not be reached in batch conditions. It was therefore necessary to feed the reactor continuously with solution in order to keep the concentration of the reactive species constant and allow the establishment of steady state. The first objective of the eCTR characterization was to verify that the continuous axial flow induced by the recirculation did not significantly disturb the hydrodynamics. This check was carried out without rotation of the internal cylinder in order to be in the most sensitive conditions possible.

Cyclic voltammetries (CV) were performed at 5 mV.s^{-1} in phosphate solution that contained hexacyanoferrate (III) and hexacyanoferrate (II) each at 1 mM. The CV records (current intensity as a function of potential) were compared using the oxidative part ($I > 0\ A$) because the reductive part may be biased by the reduction of oxygen, which occurs in a similar potential range as the reduction of hexacyanoferrate (III). The CV records were compared with two characteristic values: the current at the peak (I_P) and the limiting current (I_L) measured at upper limit of the potential scan from 0.55 to 0.6 V/SCE (see Figure 4). Eight electrodes were individually addressed in this experiment (electrodes c-e-h-j-m-o-r-t, see Materials and Methods section). The 8 electrodes gave highly reproducible CV records (Figure S1 in Supplementary data) with standard deviation lower than 4% and 5% for the I_P and I_L values, respectively.

CV were recorded in batch condition (no solution flow) and in continuous flow of 700 mL.h^{-1} (corresponding to a superficial velocity of 4.4 cm.h^{-1}). No significant difference was observed on the general shape of the CV recorded with or without continuous flow. In batch condition, I_P and I_L were 2.8 ± 0.2 and 0.74 ± 0.07 mA, respectively; while, in continuous mode they were 2.8 ± 0.2 and 0.71 ± 0.07 mA, respectively. The small difference between the batch and the continuous mode on the I_P and I_L values can be neglected according to the overlap of the standard deviations. It can be concluded that the small axial velocity of 4.4 cm.h^{-1} due to the solution flow had no significant effect on the current produced by the electrodes.

Consequently, all the experiments were conducted with a continuous solution flow of 700 mL.h^{-1}, assuming that the convective part of the mass transport was fully controlled by the rotation of the inner cylinder and neglecting the influence of the small axial flow.

4.1.2. Nernst layer thickness without rotation

CV were performed at 1 mV.s^{-1} in phosphate solution that contained hexacyanoferrate (III) and hexacyanoferrate (II) at equal concentrations ranging from 0 to 20 mM. The Figure 3 shows a correct linear relationship between the I_L values extracted from the CV curves and the hexacyanoferrate (II) concentrations, with a slope of 0.21 A.m^3.mol^{-1}. According to the Nernst hypothesis, this slope value corresponds to a Nernst diffusion layer thickness δ_N of 423 µm (equation 15 with 5.09×10^{-10}m^2.s^{-1} for the hexacyanoferrate (II) diffusion coefficient and 18 cm^2 for the electrode surface area).

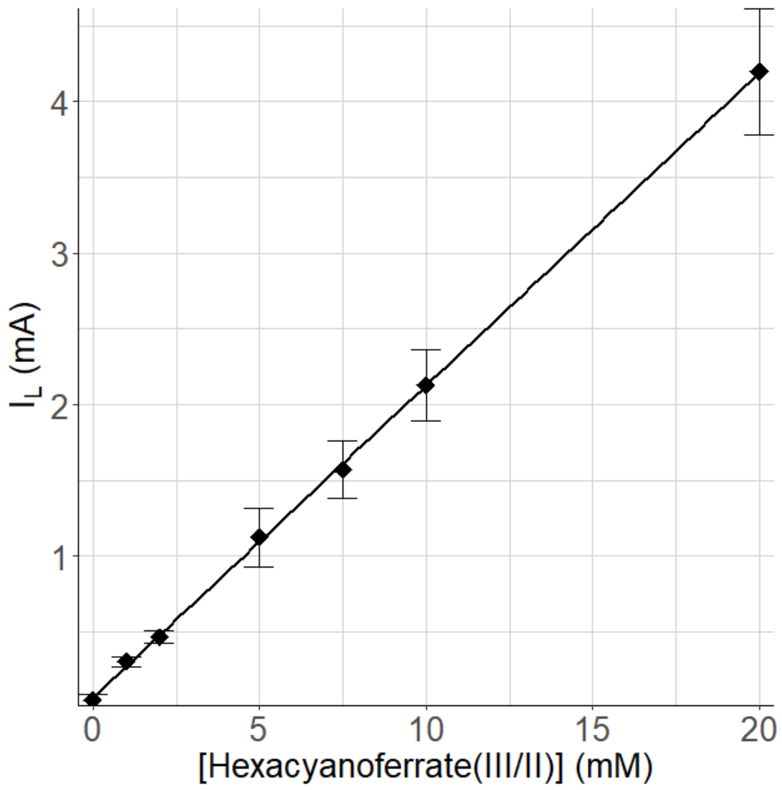

Figure 3: Experimental relation between I_L and the hexacyanoferrate (II) concentration without rotation of the inner cylinder; I_L values were obtained from the CV recorded at 1 mV.s^{-1}; average values and standard deviations resulted from CV performed on 15 electrodes. The regression line corresponds to $I_L = 0.07 + 0.21C_b$ with $R^2 = 0.9995$.

In fact, from a fully rigorous theoretical standpoint, the Nernst hypothesis should not be used in the absence of stirring, as it was the case here, but the equation of semi-infinite linear diffusion should be applied. Nevertheless, the estimation of a Nernst layer thickness is a relevant criterion for evaluating possible hydrodynamic disturbance at the electrode surface. In quiescent solution, parasite stirring may occur due to natural convection or parasitic motion, vibrations transmitted to the reactor for example. In quiescent condition, the thickness of the Nernst layer is typically in the range of a few hundreds of µm; values ranging from 100 to 500 µm have been reported in the literature [58–60]. The high value of 423 m obtained here confirmed that the continuous solution flow did not induce parasitic motion of the solution near the electrode surface.

4.2. Impact of hydrodynamics on the current produced by hexacyanoferrate (II) oxidation

4.2.1. Correction of the effect electrode rotation on the current measured

With the rotation of the inner cylinder, the CV records were of extremely poor quality because of large discrepancy in the values of the current measured. By increasing the measurement frequency in order to monitor the rapid current variations, it was observed that the current was disturbed in a regular periodic way, with a period corresponding to the time for a complete rotation of the cylinder. The reference electrode was located at a fixed point in the crown between the inner and outer cylinders (Figure 1). Each working electrode, 1 cm wide, represented a small section of the inner cylinder. As the cylinder rotated, the distance of each working electrode from the reference varied from about 2 cm, when facing the reference, to half a circumference (around 24 cm) when facing the opposite direction. The periodic variation of the distance of the working electrode from the reference induced the periodic variation of the potential of the working electrode, which was responsible for the periodic variation of the current measured.

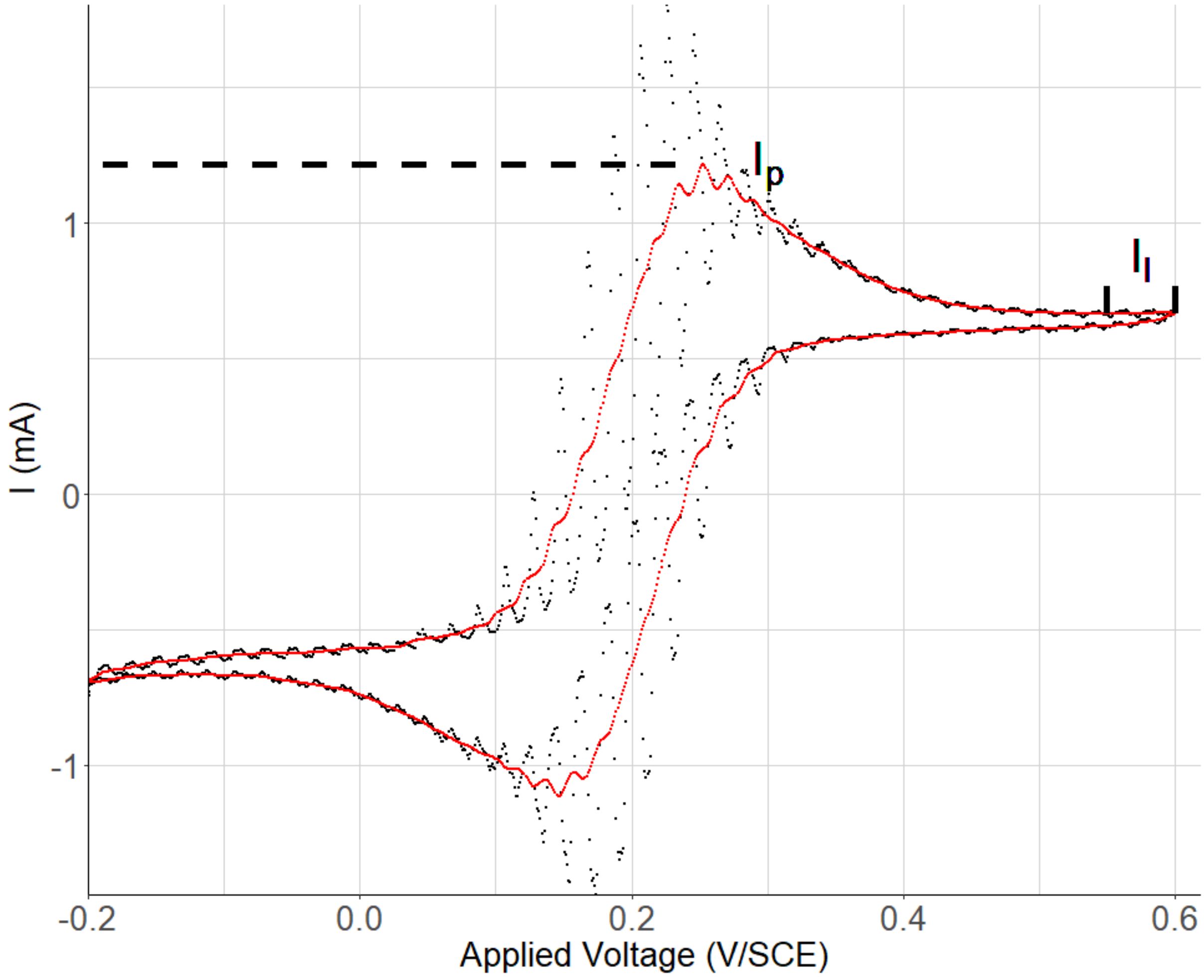

Figure 4: Numerical processing of the CV records. Raw data (black) obtained from the second CV cycle of the anode *i* immersed in hexacyanoferrate (III/II) 1mM with supporting electrolyte, with a flow rate of 700 mL.h^{-1}. CV was performed using a scan rate of 1 mV.s^{-1} and the inner cylinder rotated at 3 RPM. Fitted curve (red) after applying a moving average on $\Delta V = 20$ mV.rot^{-1}. Value of $I_P$and I_L represented.

This periodic perturbation of the current was corrected by numerically processing the raw data. On Figure 4, an example of raw data is given (black points) and the same curve is represented after applying a moving average correction (red curve). The moving average correction was performed on the Volt interval ΔV, which corresponded to the potential range that was scanned during one rotation of the inner cylinder. ΔV expressed in V.rot^{-1} corresponded to the ratio of the scan rate σ (V.s^{-1}) to the rotation speed of the inner cylinder ω (RPM):

$$\Delta V = \frac{\sigma \times 60}{\omega} \tag{31}$$

This correction was systematically used to interpret the CV records and extract the characteristic values I_p and I_L.

4.2.2. Determination of the limiting currents as a function of rotation speed

CV were recorded at 1 mV.s^{-1} in phosphate solutions that contained equal concentrations of hexacyanoferrate(II) and hexacyanoferrate(III) ranging from 0 to 20 mM. The eCTR was continuously fed with the solution at 700 mL.h^{-1}. The inner cylinder rotated at different speeds from 1 to 200 RPM, which gave complete picture of the wavy vortex and turbulent vortex flow regimes (Table 1). The limiting current I_L was measured as the mean value of the oxidative plateau of the CV records observed at the upper values of the potential. I_L was represented as a function of the concentration of hexacyanoferrate(II) in the bulk for different rotation speeds (Figure 5A). The average values and standard deviations were calculated from the measurements obtained from the 15 individually addressed electrodes, which were implemented for each experimental condition.

In most cases, the CV records presented the well-known current peaks (in both oxidation and reduction parts of the CV), which showed the transient rate-limiting effect of mass transfer during the potential scan (Figure 5B). Considering the oxidation part ($I > 0$ A), during the scan in the positive direction, when the potential applied to the working electrode became higher than the equilibrium potential, oxidation at the electrode surface consumed the electroactive species, leading to the formation of the diffusive layer. When the applied potential increased quickly, high transient currents were produced, but mass transfer was not able to provide a sufficiently high flow of electroactive species to balance the electrochemical consumption, and consequently the current decreased. This is the reason of the current peak observed at low hexacyanoferrate (II) concentrations and low rotating speeds. In contrast, at high hexacyanoferrate (II) concentrations and high rotating speeds, mass transport was more efficient and able to compensate the consumption of the electroactive species, so that a stationary state was reached in a large range of the potential scan. The transient peak vanished as the concentration and the rotating speed increased (Figure 5C).

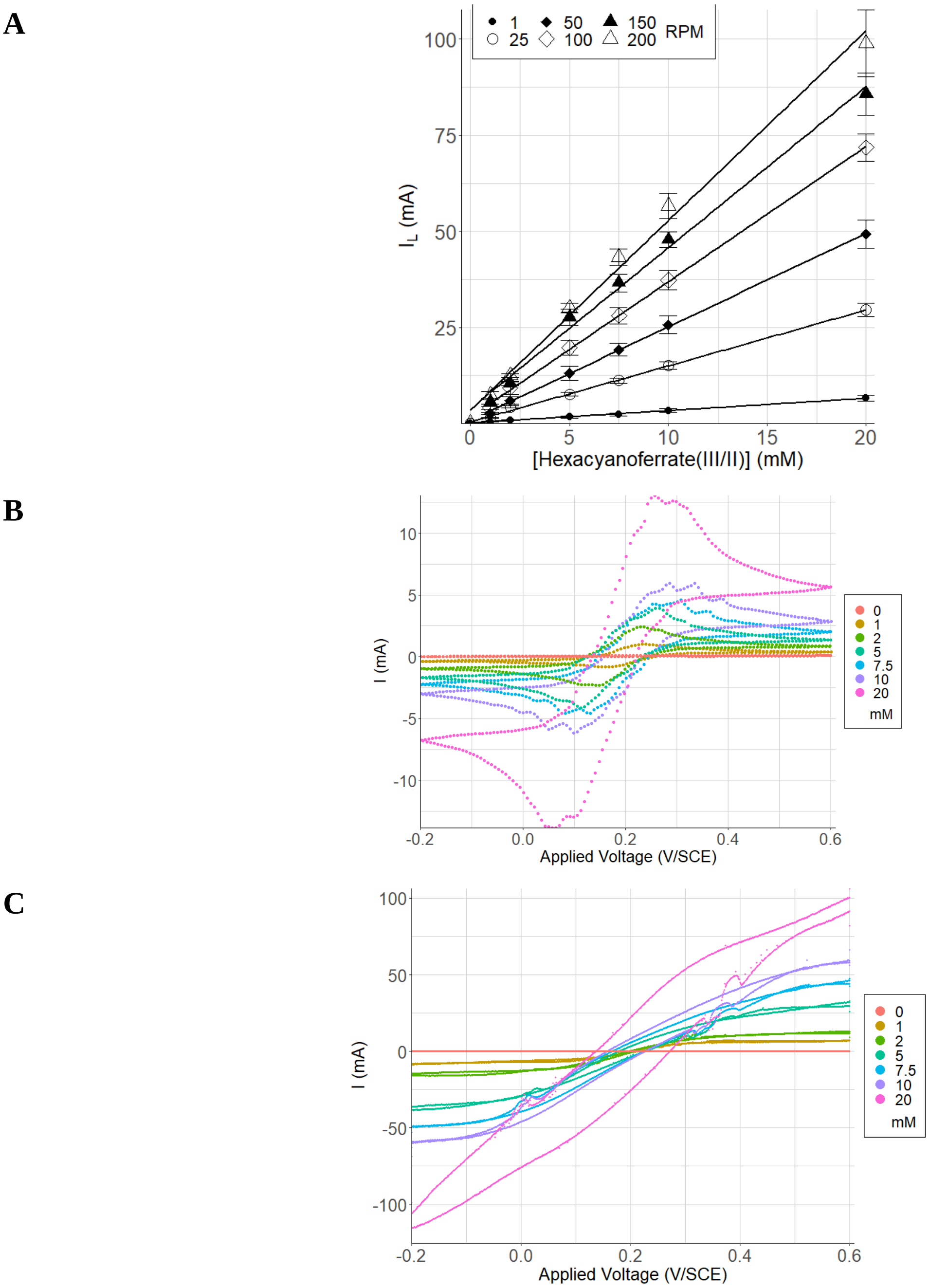

Figure 5: CV recorded with various hexacyanoferrate (III/II) concentrations and various rotating speeds of the inner cylinder; only 6 rotation speeds are plotted among the 13 tested; equation of the regression lines and the R^2 values are given in Supplementary Data Table S1. A) I_L values as a function of hexacyanoferrate (II) concentration; average and standard deviations resulted from the measures of 15 electrodes. B) CV curves from electrode *c* at 1 RPM and C) at 200 RPM.

In any cases, when the potential is high enough, only mass transfer was rate-limiting and the value of the current did no longer depend on the value of the potential; the current displayed a horizontal plateau on the CV records. Obtaining the I_L value was not obvious for the highest concentration (20 mM) and at high rotating speed (≥ 150 RPM) because, in these conditions, mass transport tended to be less rate-limiting. The potential of the upper limit of the CV scan was not high enough to rigorously reach the horizontal plateau that characterizes the limiting current (Figure 5C). Nevertheless, it was not possible to use higher values of potential without reaching the water oxidation range. In this case, I_L was assessed as the value of the current at the highest potential value. I_L tended thus to be slightly underestimated for the highest concentration value at the highest rotating speeds. Nevertheless, it can be observed in Figure 5A that the deviation from the linear regression was very limited. These values were consequently kept for further analysis but some precautions were taken when using these data.

4.3. Evolution of the diffusive layer thickness with hydrodynamics: evidencing the impact of wavy (WVF) and turbulent vortex flow (TVF)

The eCTR was operated in the rotation speed range from 1 to 200 RPM, corresponding to Taylor numbers from 144 to 28,793 (i.e. $2.7Ta_c < Ta < 544Ta_c$) allowing to cover different hydrodynamic regimes from the wavy vortex to turbulent vortex flows (see Table 1). To analyze the impact of the hydrodynamic regime on the electrochemical reactions, the limiting current I_L was represented as a function of ω using a log scale for the different selected concentrations of hexacyanoferrate (II) (Figure 6A).

Without any electroactive species, the velocity had no significant effect on the limiting current ($I_{L0mM} \approx 70$ µA for each ω), showing that the residual currents were likely due to adsorbed species rather than soluble species contained in solution. For each concentration from 1 to 20 mM, a log-linear increase of the limiting current with the rotation speed was observed, highlighting the decrease in the limitation due to mass transfer. To illustrate the influence of hydrodynamics independently of the concentration of the reactive species, the Nernst-diffusive layer thickness (δ_N) is calculated using equation 15 (Figure 6B) and by considering $I_L - I_{L0mM}$ for the calculation. Figure 6B presents the diffusion layer thickness δ_N calculated from the experimental data as a function of the rotation speed ω using a log scale. A significant difference is observed between the curve for a concentration of hexacyanoferrate (II) of 2 mM and the other concentrations. This difference could be linked to an experimental bias for intermediate rotation speed from 5 to 50 RPM. Consequently, this concentration is no longer considered for further data exploitation.

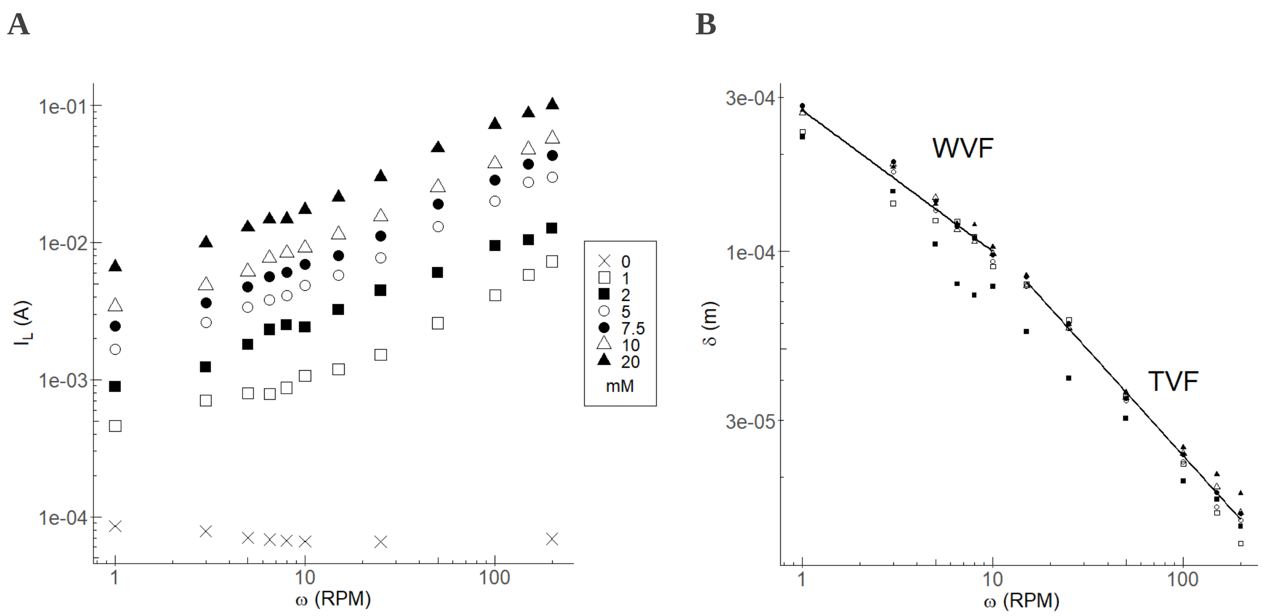

Figure 6: A) Effect of the angular velocity on the I_L value obtained on CV at various concentrations of hexacyanoferrate (II) B) Effect of the angular velocity on the diffusive layer thickness. Data recorded at 2 mM are represented in the graph but they were excluded from the regressions. WVF: Wavy Vortex Flow; TVF: Turbulent Vortex Flow. Data are represented on a log scale; each point is the average value obtained from 15 electrodes.

The increase in the rotation speed of the inner cylinder induced a velocity profile gradient along the gap between the two cylinders with a maximum velocity near the inner cylinder where the anodic reaction was located. As expected, δ_N decreased with higher rotation speed.

Moreover, by considering the experimental points for all concentrations, two distinct linear evolutions are observed, with a modification of the slope for a rotation speed in the range from 10 to 15 RPM. This slope break showed the transition between the wavy vortex and the turbulent vortex flows, and confirms the boundary of 40 Ta_c (corresponding to 14.8 RPM).

For each identified flow regimes (WVF and TVF for $\omega < 10\,RPM$ and $\omega > 15\,RPM$ respectively), the Nernst-diffusive layer thickness (and the associated limited current I_L) varied with the rotation speed according to a power law, as expected from the theory for laminar and turbulent flows in equations 19 and 28:

$$\delta_N = 10^{-K}\,\omega^{-\alpha} \tag{32}$$

Values of K and α resulting from numerical fitting of the experimental data are provided in Table 2. For 10 and 20 mM, K and α values may be underestimated considering the approximation in the calculation of the $I_L$value shown in 3.2.2. for high concentration and high velocities. Nonetheless, they followed the same tendency as for the other concentrations. The value of α

coefficient (0.44 and 0.66 for WVF and TVF respectively), is more sensitive to the modification of the flow regime than the coefficient K (3.99 and 3.97 for WVF and TVF respectively). Its dependency on the flow regime is linked to the difference in the physical nature of the flows, from a more structured one for the WVF to a more heterogeneous and chaotic flow for the TVF one. Those results help describing the two different Couette-Taylor vortex flows by estimating the Nernst-diffusive layer thickness using electrochemical tools and confirmed the boundary value between these two regimes.

Table 2: Values of the experimental coefficient of the log correlation of the diffusive layer and the concentration of the electroactive species $\delta_N = 10^{-K}\,\omega^{-\alpha}$. Values are given for each concentration, for the total dataset or by removing the 10 and 20 mM concentrations.

Hexacyanoferrate (III/II) (mM)	Wavy Vortex Flow			Turbulent Vortex Flow		
	K_{WVF}	α_{WVF}	R^2	K_{TVF}	α_{TVF}	R^2
1	4.0	0.38	0.96	3.9	0.73	1.00
5	4.0	0.47	1.00	4.0	0.66	1.00
7.5	4.0	0.47	0.99	4.0	0.66	1.00
10	4.0	0.45	0.98	4.0	0.63	1.00
20	4.0	0.42	0.99	4.0	0.60	1.00
Total set	4.0	0.44	0.96	4.0	0.66	0.99
Total set (without 10 and 20 mM)	4.0	0.44	0.96	4.0	0.68	0.99

5. Discussion

5.1. Flow characterization using micro-electrodes in CTR

The study of Couette-Taylor hydrodynamics has already been carried out using microelectrodes integrated in the outer cylinder. Sobolík *et al.* [48,61] characterized axial and azimuthal components of the shear rate on the wall of the outer cylinder of a CTR using a microelectrode. They measured the limiting current I_L with the three-segment microelectrodes on the surface of the outer cylinder and deduced the shear rate ($\dot{\gamma}$) and the associated shear stress ($\tau = \mu\dot{\gamma}$) from the rotation speed of the inner cylinder. Under laminar condition, their results confirmed the theoretical evolution of the limiting current according to shear rate $I_L \propto \dot{\gamma}^n$ (equation 18 for shear rate in the range 4 – 80 s^{-1}) with an experimentally determined value $n = 0.31$ (close to the theoretical value of 0.33).

As the fluid velocity is directly linked to shear rate τ in Couette-Taylor flows (equation 7, 8 or 9 depending on the flow regime), it is possible to express the limiting current obtained by Sobolík *et al.* [48,61] as a function of the rotation speed for wavy vortex flows, in the form $I_L \propto \omega^{\alpha}$. It gave $\alpha = 0.45$ considering equation 8 for the shear rate range tested. The same approach has been considered by Berrich *et al.* [49] with the same parameter values n for the calculation of the shear rates giving the components of the vortices on the outer wall using more electrodes.

Those results obtained under wavy vortex conditions showed similar values of α (0.45) than the results presented here on the rotating inner cylinder (0.44). Considering non-laminar conditions by comparison of the theoretical value of Gabe & Robison [52], this tends to show the major effect of vortices on the electrochemical reactions next to the walls of CTR, even next to the outer wall due to the divergence with laminar theoretical behavior.

The approach used in our work with large and numerous electrodes shows also reliable and reproducible results such as the ones obtain with much precise electrodes used for precise understanding of hydrodynamics in CTR.

5.2.Comparison between RCE and CTR with literature experimental and theoretical results

Rotating cylinder electrode (RCE) are reactors in which a cylinder is rotating in the electrolyte with no influence of the outer wall of the reactor on the flow [34]. A RCE could thus be considered as a CTR with a so small radius ratio (R_i/R_o) that the impact of the outer cylinder can be neglected. In comparison, CTR are characterized by the major influence of the outer wall on the flow and with conversely high radius ratio. It is generally observed in literature that Couette-Taylor flows appear from a radius ratio of 0.5 giving typical RCE with radius ratio bellow this value [40,62]. It is still necessary to investigate those flow differences on electrochemical reactions.

Correlations have been established on different devices between the Sherwood numbers and the Reynolds numbers as shown in Figure 7. For comparison, Sherwood numbers were calculated from the present work (equation 4) by using the average value of Nernst-diffusive layer for each rotation speed.

Former work has been done to characterize the influence of mass transfer in RCE [35]. One of the main study focused on hydrodynamic in RCE was proposed by Eisenberg *et al.* [34]. They considered the effect of various geometries (with radius ratio from 0.2 to 0.4) and Reynolds number 1,000 to 100,000 (corresponding to the range from 4.6 to 460 RPM for the eCTR presented in this study). They characterized mass transfer on the rotating cylinder-electrode surface. Eisenberg *et al.* [34] gave an α value only different by 6% from the data under turbulent vortex flow from present study in Figure 7 (from equation 32). Thus, the present work gave similar results to those in RCE for turbulent flows due to the lower influence of the fixed outer cylinder on hydrodynamics at inner cylinder wall under turbulent regime.

A mass transfer analysis of a CTR was also made electrochemically by Legrand *et al.* [50] with an inner cylinder containing both cathode and anode in a device with a radius ratio of 0.8 (gap between the two cylinders of 5 mm) with *Ta* values from 200 to 1600 (corresponding to values from 1.4 to 11 RPM in this study). They followed the impact of vortices and axial flow on the reduction reaction that occurred on the inner cylinder rotating electrode by measuring the Sherwood number. Without axial flow, i.e. for equivalent operating conditions than in the present study, Sherwood expression reveals similar behavior in the *Re* range corresponding to wavy vortex flow ($Re < 2400$). They was a mean difference in Sherwood numbers from empirical correlation of Legrand *et al.* [50] and the experimental points of 13% (with maximal difference of 15% for 8 RPM) related to experimental measurement accuracy and reproducibility.

The *Sh* versus *Re* correlations calculated from the theoretical models of Gabe & Robinson [52,53] (equation 21 and 30) are also presented in Figure 7. The parameter B from equation 30 was estimated to $B = 5.71 \times 10^{-3}\ [-]$ using the experimental data under turbulent vortex flows. The correlations are represented with dotted lines for a large range in terms of Reynolds number even if they are only applicable in strictly laminar and turbulent flow respectively.

The theoretical model of Gabe & Robinson [52,53] states two different behaviors. The Figure 7 shows an excellent correspondence between the experimental points for turbulent vortex flows and this theoretical model. The hypothesis made by to establish their equations for the turbulent flows could therefore be applied to data obtained in turbulent vortex flow. In this regime, the main part of the mass transport is due to the turbulence. Likewise, results from Eisenberg *et al.* [34] also follow this tendency and could corroborate the negligible part of the vortex transport in turbulent vortex flow.

A different behavior appears for wavy vortex flow, which was not described theoretically [52]. The data recorded at this regime match neither the theoretical curves for the laminar flow nor those for the turbulent flow. It emphasizes the impact of another phenomenon than the ones described theoretically for *Re* values that may be due to vortices. Sherwood numbers are also slightly higher in the experimental approach under wavy vortex flows than in the laminar theory, which corroborates the role of the vortex in increasing the transfer close to the electrode surface for such rotation speeds (Figure 7).

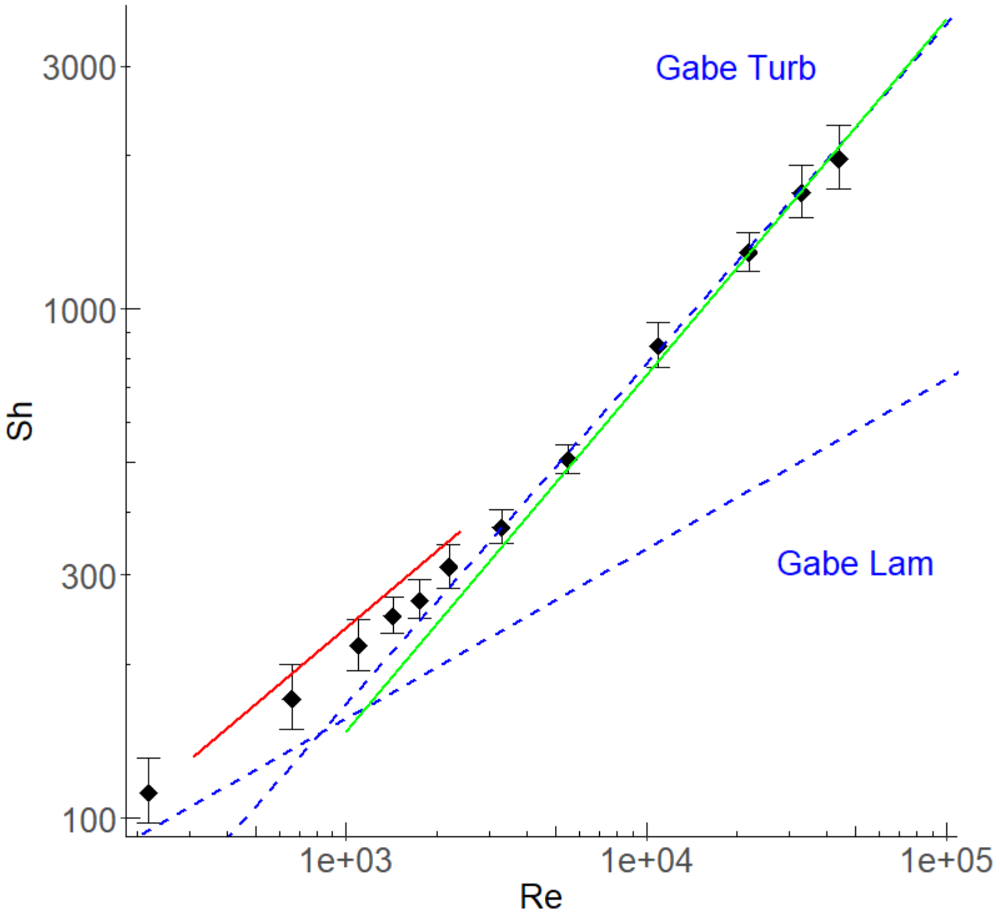

Figure 7: Sherwood number (*Sh*) as a function of Reynolds number (*Re*). Comparison of correlations from Eisenberg *et al.* [34] in green, in the CTR of Legrand *et al.* [50] in red and with the theoretical equations of Gabe & Robinson [52,53] in dashed blue using $B = 5.71 \times 10^{-3} [-]$), versus the experimental data (♦ obtained with the 5 concentrations for the 15 electrodes).

The eCTR developed here gave results that matched the experimental and theoretical results reported in the literature for identical flow regimes. Moreover, it enriches the former results by characterizing the wavy vortex regimes, which were clearly distinct from the turbulent vortex flows.

5.3. Characterization of coupled fluid dynamics and electrochemical modelling in Couette-Taylor vortex flows

The range of Couette-Taylor flows is described in Table 3 and it allows having a new point of view on the transition between vortices and turbulence besides their impact on electrochemical reactions.

The present eCTR allowed the control of diffusive layer thickness going from 15 to 423 µm (Table 3). For microbial electrochemical processes, this thickness range is interesting regarding the thickness of electroactive biofilms, which commonly ranges from 20 to 250 µm [63–65]. Indeed, shear stress is a promising way to control biofilm development [38,66], coupled to the control of mass transfer close to the electrode. The shear stress is also known as an important factor that influences biofilm structural properties [39,41,42]. In non-electroactive biofilms, increased shear is known to enhance particle detachment at the surface of the biofilm, which often lead to the formation of a thin and dense biofilm [38,66]. Nevertheless, such investigations are rarely done on electroactive biofilms. The eCTR developed here allowed applying a range of shear stress from 10^{-4} to 10 Pa (from equation 7 and 9) versus 10^{-1} to 10^2 for the RCE [37]. These shear stress values can be applied to up to 20 biofilm duplicates developed in exactly the same hydrodynamics condition. This should be a powerful tool to explore the influence of shear stress on the formation, maturation, electrochemical efficiency and, possibly, regeneration of electroactive biofilms [67].

Table 3: Key parameters of the study

Flow characteristics	Taylor range	Rotation speed (RPM)	Nernst diffusive layer thickness (µm)	Shear stress (mPa)	α value
No rotation	Ta=0, Axial flow≈0	0	423	$\tau \approx 0$	NA
WVF	$140 \leq Ta \leq 2100$	$1 \leq \omega \leq 14.8$	$274 \geq \delta_N \geq 84.5$	$0.1 \leq \tau \leq 40$	0.44
TVF	$2100 \leq Ta \leq 29000$	$14.8 \leq \omega \leq 200$	$80.4 \geq \delta_N \geq 14.6$	$40 \leq \tau \leq 2700$	0.66

6. Conclusion

The proposed eCTRreactor is able to describe electrochemical kinetics in controlled hydrodynamic conditions decoupled from the flow input for low axial flow rates. Results are repeatable on the 16 electrodes connected that will help characterizing the influence of hydrodynamics on electroactive biofilms allowing performing conveniently replicates. The big size planar electrodes give a large electroactive surface to develop biofilms in the same hydrodynamics conditions and will allow sampling representative part of whole biofilm for comprehensive analysis during long-term experiments.

The characterization of the electrochemical response has been made as a function of the flow regime. The electrochemical diffusive layer thickness (δ_N) on the surface of the inner cylinder were extracted from the limiting current values (I_L) and correlated to the rotation speed of the inner cylinder. Those relations are given as function of the Couette-Taylor flow regime and are then linked to the shear stress resulting from hydrodynamics. Such characterization is necessary to further understand how biofilm development can affect electrochemical response.

The CTR vortices influence deeply electrochemical behavior for lower fluid dynamics. The vortices are responsible of the main part of the mass transport under the wavy vortex flow while the turbulence is responsible of most of the mass transport in the turbulent vortex flow. Results of this study contribute to better understand the role of fluid dynamics on electrochemical reactions in Couette-Taylor reactors.

References

[1] Z.W. Seh, J. Kibsgaard, C.F. Dickens, I.B. Chorkendorff, J.K. Norskov, T.F. Jaramillo, Combining theory and experiment in electrocatalysis: Insights into materials design, Science. 355 (2017) eaad4998. https://doi.org/10.1126/science.aad4998.

[2] D. Larcher, J.-M. Tarascon, Towards greener and more sustainable batteries for electrical energy storage, Nat. Chem. 7 (2015) 19–29. https://doi.org/10.1038/NCHEM.2085.

[3] S. Kumar, G. Saeed, L. Zhu, K.N. Hui, N.H. Kim, J.H. Lee, 0D to 3D carbon-based networks combined with pseudocapacitive electrode material for high energy density supercapacitor: A review, Chem. Eng. J. 403 (2021) 126352. https://doi.org/10.1016/j.cej.2020.126352.

[4] C. Santhosh, V. Velmurugan, G. Jacob, S.K. Jeong, A.N. Grace, A. Bhatnagar, Role of nanomaterials in water treatment applications: A review, Chem. Eng. J. 306 (2016) 1116–1137. https://doi.org/10.1016/j.cej.2016.08.053.

[5] Y. Li, D. Xu, C. Chen, X. Li, R. Jia, D. Zhang, W. Sand, F. Wang, T. Gu, Anaerobic microbiologically influenced corrosion mechanisms interpreted using bioenergetics and bioelectrochemistry: A review, J. Mater. Sci. Technol. 34 (2018) 1713–1718. https://doi.org/10.1016/j.jmst.2018.02.023.

[6] A. Al-Mamun, W. Ahmad, M.S. Baawain, M. Khadem, B.R. Dhar, A review of microbial desalination cell technology: Configurations, optimization and applications, J. Clean. Prod. 183 (2018) 458–480. https://doi.org/10.1016/j.jclepro.2018.02.054.

[7] P. Dessi, L. Rovira-Alsina, C. Sanchez, G.K. Dinesh, W. Tong, P. Chatterjee, M. Tedesco, P. Farras, H.M.V. Hamelers, S. Puig, Microbial electrosynthesis: Towards sustainable biorefineries for production of green chemicals from CO2 emissions, Biotechnol. Adv. 46 (2021) 107675. https://doi.org/10.1016/j.biotechadv.2020.107675.

[8] H. Wang, Z.J. Ren, A comprehensive review of microbial electrochemical systems as a platform technology, Biotechnol. Adv. 31 (2013) 1796–1807. https://doi.org/10.1016/j.biotechadv.2013.10.001.

[9] C. Santoro, C. Arbizzani, B. Erable, I. Ieropoulos, Microbial fuel cells: From fundamentals to applications. A review, J. Power Sources. 356 (2017) 225–244. https://doi.org/10.1016/j.jpowsour.2017.03.109.

[10] B.E. Logan, K. Rabaey, Conversion of Wastes into Bioelectricity and Chemicals by Using Microbial Electrochemical Technologies, Science. 337 (2012) 686–690. https://doi.org/10.1126/science.1217412.

[11] H. Dau, C. Limberg, T. Reier, M. Risch, S. Roggan, P. Strasser, The Mechanism of Water Oxidation: From Electrolysis via Homogeneous to Biological Catalysis, ChemCatChem. 2 (2010) 724–761. https://doi.org/10.1002/cctc.201000126.

[12] O. Modin, F. Aulenta, Three promising applications of microbial electrochemistry for the water sector, Environ. Sci. Water Res. Technol. 3 (2017) 391–402. https://doi.org/10.1039/C6EW00325G.

[13] J. Zhao, F. Li, Y. Cao, X. Zhang, T. Chen, H. Song, Z. Wang, Microbial extracellular electron transfer and strategies for engineering electroactive microorganisms, Biotechnol. Adv. 53 (2021) 107682. https://doi.org/10.1016/j.biotechadv.2020.107682.

[14] R. Kumar, L. Singh, A.W. Zularisam, Exoelectrogens: Recent advances in molecular drivers involved in extracellular electron transfer and strategies used to improve it for microbial fuel cell applications, Renew. Sustain. Energy Rev. 56 (2016) 1322–1336. https://doi.org/10.1016/j.rser.2015.12.029.

[15] K. Guo, A. Prévoteau, S.A. Patil, K. Rabaey, Materials and Their Surface Modification for Use as Anode in Microbial Bioelectrochemical Systems, in: Funct. Electrodes Enzym. Microb. Electrochem. Syst., WORLD SCIENTIFIC (EUROPE), 2017: pp. 403–427. https://doi.org/10.1142/9781786343543_0011.

[16] T.R. Molderez, A. Prévoteau, F. Ceyssens, M. Verhelst, K. Rabaey, A chip-based 128-channel potentiostat for high-throughput studies of bioelectrochemical systems: Optimal electrode potentials for anodic biofilms, Biosens. Bioelectron. 174 (2021) 112813. https://doi.org/10.1016/j.bios.2020.112813.

[17] R. Rousseau, L. Etcheverry, E. Roubaud, R. Basseguy, M.-L. Delia, A. Bergel, Microbial electrolysis cell (MEC): Strengths, weaknesses and research needs from electrochemical engineering standpoint, Appl. Energy. 257 (2020) 113938. https://doi.org/10.1016/j.apenergy.2019.113938.

[18] B.G. Lusk, P. Parameswaran, S.C. Popat, B.E. Rittmann, C.I. Torres, The effect of pH and buffer concentration on anode biofilms of Thermincola ferriacetica, Bioelectrochemistry. 112 (2016) 47–52. https://doi.org/10.1016/j.bioelechem.2016.07.007.

[19] C. Moss, N. Jarmatz, D. Hartig, L. Schnoeing, S. Scholl, U. Schroeder, Studying the Impact of Wall Shear Stress on the Development and Performance of Electrochemically Active Biofilms, Chempluschem. 85 (2020) 2298–2307. https://doi.org/10.1002/cplu.202000544.

[20] M.A. Islam, B. Ehiraj, C.K. Cheng, B.N. Dubey, M.M.R. Khan, Biofilm re-vitalization using hydrodynamic shear stress for stable power generation in microbial fuel cell, J. Electroanal. Chem. 844 (2019) 14–22. https://doi.org/10.1016/j.jelechem.2019.05.013.

[21] A.-A.D. Jones, C.R. Buie, Continuous shear stress alters metabolism, mass-transport, and growth in electroactive biofilms independent of surface substrate transport, Sci. Rep. 9 (2019) 2602. https://doi.org/10.1038/s41598-019-39267-2.

[22] M.A. Amirdehi, L. Gong, N. Khodaparastasgarabad, J.M. Sonawane, B.E. Logan, J. Greener, Hydrodynamic interventions and measurement protocols to quantify and mitigate power overshoot in microbial fuel cells using microfluidics, Electrochimica Acta. 405 (2022) 139771. https://doi.org/10.1016/j.electacta.2021.139771.

[23] T. Krieg, J.A. Wood, K.-M. Mangold, D. Holtmann, Mass transport limitations in microbial fuel cells: Impact of flow configurations, Biochem. Eng. J. 138 (2018) 172–178. https://doi.org/10.1016/j.bej.2018.07.017.

[24] T. Noël, Y. Cao, G. Laudadio, The Fundamentals Behind the Use of Flow Reactors in Electrochemistry, Acc. Chem. Res. 52 (2019) 2858–2869. https://doi.org/10.1021/acs.accounts.9b00412.

[25] B.J. Adesokan, X. Quan, A. Evgrafov, A. Heiskanen, A. Boisen, M.P. Sørensen, Experimentation and numerical modeling of cyclic voltammetry for electrochemical micro-sized sensors under the influence of electrolyte flow, J. Electroanal. Chem. 763 (2016) 141–148. https://doi.org/10.1016/j.jelechem.2015.12.029.

[26] H. Ren, C.I. Torres, P. Parameswaran, B.E. Rittmann, J. Chae, Improved current and power density with a micro-scale microbial fuel cell due to a small characteristic length, Biosens. Bioelectron. 61 (2014) 587–592. https://doi.org/10.1016/j.bios.2014.05.037.

[27] M.Z. Bazant, K. Thornton, A. Ajdari, Diffuse-charge dynamics in electrochemical systems, Phys. Rev. E. 70 (2004) 021506. https://doi.org/10.1103/PhysRevE.70.021506.

[28] C. Picioreanu, J.S. Vrouwenvelder, M.C.M. van Loosdrecht, Three-dimensional modeling of biofouling and fluid dynamics in feed spacer channels of membrane devices, J. Membr. Sci. 345 (2009) 340–354. https://doi.org/10.1016/j.memsci.2009.09.024.

[29] M. Böl, R.B. Möhle, M. Haesner, T.R. Neu, H. Horn, R. Krull, 3D finite element model of biofilm detachment using real biofilm structures from CLSM data, Biotechnol. Bioeng. 103 (2009) 177–186. https://doi.org/10.1002/bit.22235.

[30] S.C. Perry, C.P. de León, F.C. Walsh, Review—The Design, Performance and Continuing Development of Electrochemical Reactors for Clean Electrosynthesis, J. Electrochem. Soc. 167 (2020) 155525. https://doi.org/10.1149/1945-7111/abc58e.

[31] A.N. Colli, J.M. Bisang, Time-dependent mass-transfer behaviour under laminar and turbulent flow conditions in rotating electrodes: A CFD study with analytical and experimental validation, Int. J. Heat Mass Transf. 137 (2019) 835–846. https://doi.org/10.1016/j.ijheatmasstransfer.2019.03.152.

[32] V.G. Levich, Physicochemical hydrodynamics., Prentice-Hall, Englewood Cliffs, N.J, 1962.

[33] D. Herbert-Guillou, B. Tribollet, D. Festy, Influence of the hydrodynamics on the biofilm formation by mass transport analysis, Bioelectrochemistry. 53 (2001) 119–125. https://doi.org/10.1016/S0302-4598(00)00121-5.

[34] M. Eisenberg, C.W. Tobias, C.R. Wilke, Ionic Mass Transfer and Concentration Polarization at Rotating Electrodes, J. Electrochem. Soc. 101 (1954) 306. https://doi.org/10.1149/1.2781252.

[35] F.C. Walsh, G. Kear, A.H. Nahlé, J.A. Wharton, L.F. Arenas, The rotating cylinder electrode for studies of corrosion engineering and protection of metals—An illustrated review, Corros. Sci. 123 (2017) 1–20. https://doi.org/10.1016/j.corsci.2017.03.024.

[36] D.R. Gabe, G.D. Wilcox, J. Gonzalez-Garcia, F.C. Walsh, The rotating cylinder electrode: its continued development and application, J. Appl. Electrochem. 28 (1998) 759–780. https://doi.org/10.1023/A:1003464415930.

[37] D.C. Silverman, The Rotating Cylinder Electrode for Examining Velocity-Sensitive Corrosion—A Review, Corrosion. 60 (2004) 1003–1023. https://doi.org/10.5006/1.3299215.

[38] E. Paul, J.C. Ochoa, Y. Pechaud, Y. Liu, A. Liné, Effect of shear stress and growth conditions on detachment and physical properties of biofilms, Water Res. 46 (2012) 5499–5508. https://doi.org/10.1016/j.watres.2012.07.029.

[39] A. Rochex, J.-J. Godon, N. Bernet, R. Escudie, Role of shear stress on composition, diversity and dynamics of biofilm bacterial communities, Water Res. 42 (2008) 4915–4922. https://doi.org/10.1016/j.watres.2008.09.015.

[40] M. Schrimpf, J. Esteban, H. Warmeling, T. Färber, A. Behr, A.J. Vorholt, Taylor-Couette reactor: Principles, design, and applications, AIChE J. 67 (2021) e17228. https://doi.org/10.1002/aic.17228.

[41] L.C. Simões, I.B. Gomes, H. Sousa, A. Borges, M. Simões, Biofilm formation under high shear stress increases resilience to chemical and mechanical challenges, Biofouling. 38 (2022) 1–12. https://doi.org/10.1080/08927014.2021.2006189.

[42] O. Ige, R. Barker, X. Hu, L. Umoru, A. Neville, Assessing the influence of shear stress and particle impingement on inhibitor efficiency through the application of in-situ electrochemistry in a CO2-saturated environment, Wear. 304 (2013) 49–59. https://doi.org/10.1016/j.wear.2013.04.013.

[43] L. Labraga, N. Bourabaa, T. Berkah, Wall shear stress from a rotating cylinder in cross flow using the electrochemical technique, Exp. Fluids. 33 (2002) 488–496. https://doi.org/10.1007/s00348-002-0504-x.

[44] P. Hou, T. Wang, B. Zhou, P. Song, W. Zeng, T. Muhammad, Y. Li, Variations in the microbial community of biofilms under different near-wall hydraulic shear stresses in agricultural irrigation systems, Biofouling. 36 (2020) 44–55. https://doi.org/10.1080/08927014.2020.1714600.

[45] N. Derlon, A. Masse, R. Escudie, N. Bernet, E. Paul, Stratification in the cohesion of biofilms grown under various environmental conditions, Water Res. 42 (2008) 2102–2110. https://doi.org/10.1016/j.watres.2007.11.016.

[46] N. Rizk, N. Ait-Mouheb, B. Molle, N. Roche, Treated wastewater reuse in micro-irrigation: effect of shear stress on biofilm development kinetics and chemical precipitation, Environ. Technol. 42 (2021) 206–216. https://doi.org/10.1080/09593330.2019.1625956.

[47] A. Paule, B. Lauga, L. Ten-Hage, J. Morchain, R. Duran, E. Paul, J.L. Rols, A photosynthetic rotating annular bioreactor (Taylor-Couette type flow) for phototrophic biofilm cultures, Water Res. 45 (2011) 6107–6118. https://doi.org/10.1016/j.watres.2011.09.007.

[48] V. Sobolík, B. Benabes, G. Cognet, Study of Taylor-Couette flow using a three-segment electrodiffusion probe, J. Appl. Electrochem. 25 (1995) 441–449. https://doi.org/10.1007/BF00260686.

[49] E. Berrich, F. Aloui, J. Legrand, Experimental Investigations of Couette-Taylor-Poiseuille Flows Using the Electro-Diffusional Technique, in: Vol. 1A Symp. Turbomach. Flow Simul. Optim. Appl. CFD Bio-Inspired Bio-Med. Fluid Mech. CFD Verification Valid. Dev. Appl. Immersed Bound. Methods DNS Hybrid RANSLES Methods Fluid Mach. Fluid-Struct. Interact. Flow-Induc. Noise Ind. Appl. Flow Appl. Aerosp. Act. Fluid Dyn. Flow Control — Theory Exp. Implement., American Society of Mechanical Engineers, Washington, DC, USA, 2016: p. V01AT13A013. https://doi.org/10.1115/FEDSM2016-7918.

[50] J. Legrand, P. Dumargue, F. Coeuret, Overall mass transfer to the rotating inner electrode of a concentric cylindrical reactor with axial flow, Electrochimica Acta. 25 (1980) 669–673. https://doi.org/10.1016/0013-4686(80)87074-5.

[51] F. Song, H. Koo, D. Ren, Effects of Material Properties on Bacterial Adhesion and Biofilm Formation, J. Dent. Res. 94 (2015) 1027–1034. https://doi.org/10.1177/0022034515587690.

[52] D. Gabe, D. Robinson, Mass-Transfer in a Rotating Cylinder Cell .1. Laminar-Flow, Electrochimica Acta. 17 (1972) 1121-. https://doi.org/10.1016/0013-4686(72)90028-X.

[53] D. Gabe, D. Robinson, Mass-Transfer in a Rotating Cylinder Cell .2. Turbulent-Flow, Electrochimica Acta. 17 (1972) 1129-. https://doi.org/10.1016/0013-4686(72)90029-1.

[54] A. Racina, M. Kind, Specific power input and local micromixing times in turbulent Taylor–Couette flow, Exp. Fluids. 41 (2006) 513–522. https://doi.org/10.1007/s00348-006-0178-x.

[55] A. Mehel, C. Gabillet, H. Djeridi, Bubble effect on the structures of weakly turbulent Couette Taylor Flow, in: FEDSM 2005 ASME Fluids Eng. Summer Conf., Houston, United States, 2005. https://doi.org/10.1115/1.2201641.

[56] A. Esser, S. Grossmann, Analytic expression for Taylor–Couette stability boundary, Phys. Fluids. 8 (1996) 1814–1819. https://doi.org/10.1063/1.868963.

[57] R.B. Bird, W.E. Stewart, E.N. Lightfoot, Transport Phenomena, Revised 2nd Edition, 2nd edition, Jo͡hn Wiley & Sons, Inc., New York, 2006.

[58] V.S. Bagot͡skiĭ, Fundamentals of electrochemistry, 2nd ed, Wiley-Interscience, Hoboken, N.J, 2006.

[59] A.G. Zelinsky, B.Ya. Pirogov, Effective thickness of the diffusion layer during hydrogen ion reduction in aqueous hydrochloric acid solutions, Russ. J. Electrochem. 44 (2008) 585–593. https://doi.org/10.1134/S1023193508050133.

[60] S.C. Dexter, S.H. Lin, Calculation of Seawater pH at Polarized Metal Surfaces in the Presence of Surface Films, Corrosion. 48 (1992) 50–60. https://doi.org/10.5006/1.3315918.

[61] M. Kristiawan, M.E. Hassan, A.E. Faye, V. Sobolik, Experimental investigation of Taylor-Couette-Poiseuille flow at low Taylor and Reynolds numbers, PLoS ONE. 14 (2019) e0212728. https://doi.org/10.1371/journal.pone.0212728.

[62] R.O. Monico, S.G. Huisman, T.J.G. Jannink, D.P.M. van Gils, R. Verzicco, S. Grossmann, C. Sun, D. Lohse, Optimal Taylor-Couette flow: Radius ratio dependence, J. Fluid Mech. 747 (2014) 1–29. https://doi.org/10.1017/jfm.2014.134.

[63] B.G. Lusk, P. Parameswaran, S.C. Popat, B.E. Rittmann, C.I. Torres, The effect of pH and buffer concentration on anode biofilms of Thermincola ferriacetica, Bioelectrochemistry. 112 (2016) 47–52. https://doi.org/10.1016/j.bioelechem.2016.07.007.

[64] J. Pereira, S. de Nooy, T. Sleutels, A. ter Heijne, Opportunities for visual techniques to determine characteristics and limitations of electro-active biofilms, Biotechnol. Adv. 60 (2022) 108011. https://doi.org/10.1016/j.biotechadv.2022.108011.

[65] S. Tejedor-Sanz, P. Fernández-Labrador, S. Hart, C.I. Torres, A. Esteve-Núñez, Geobacter Dominates the Inner Layers of a Stratified Biofilm on a Fluidized Anode During Brewery Wastewater Treatment, Front. Microbiol. 9 (2018). https://www.frontiersin.org/articles/10.3389/fmicb.2018.00378 (accessed January 25, 2023).

[66] P. Stoodley, Z. Lewandowski, J.D. Boyle, H.M. Lappin-Scott, Structural deformation of bacterial biofilms caused by short-term fluctuations in fluid shear: An in situ investigation of biofilm rheology, Biotechnol. Bioeng. 65 (1999) 83–92. https://doi.org/10.1002/(SICI)1097-0290(19991005)65:1<83::AID-BIT10>3.0.CO;2-B.

[67] A. Bridier, E. Desmond-Le Quemener, C. Bureau, P. Champigneux, L. Renvoise, J.-M. Audic, E. Blanchet, A. Bergel, T. Bouchez, Successive bioanode regenerations to maintain efficient current production from biowaste, Bioelectrochemistry Amst. Neth. 106 (2015) 133–140. https://doi.org/10.1016/j.bioelechem.2015.05.007.

Supplementary material

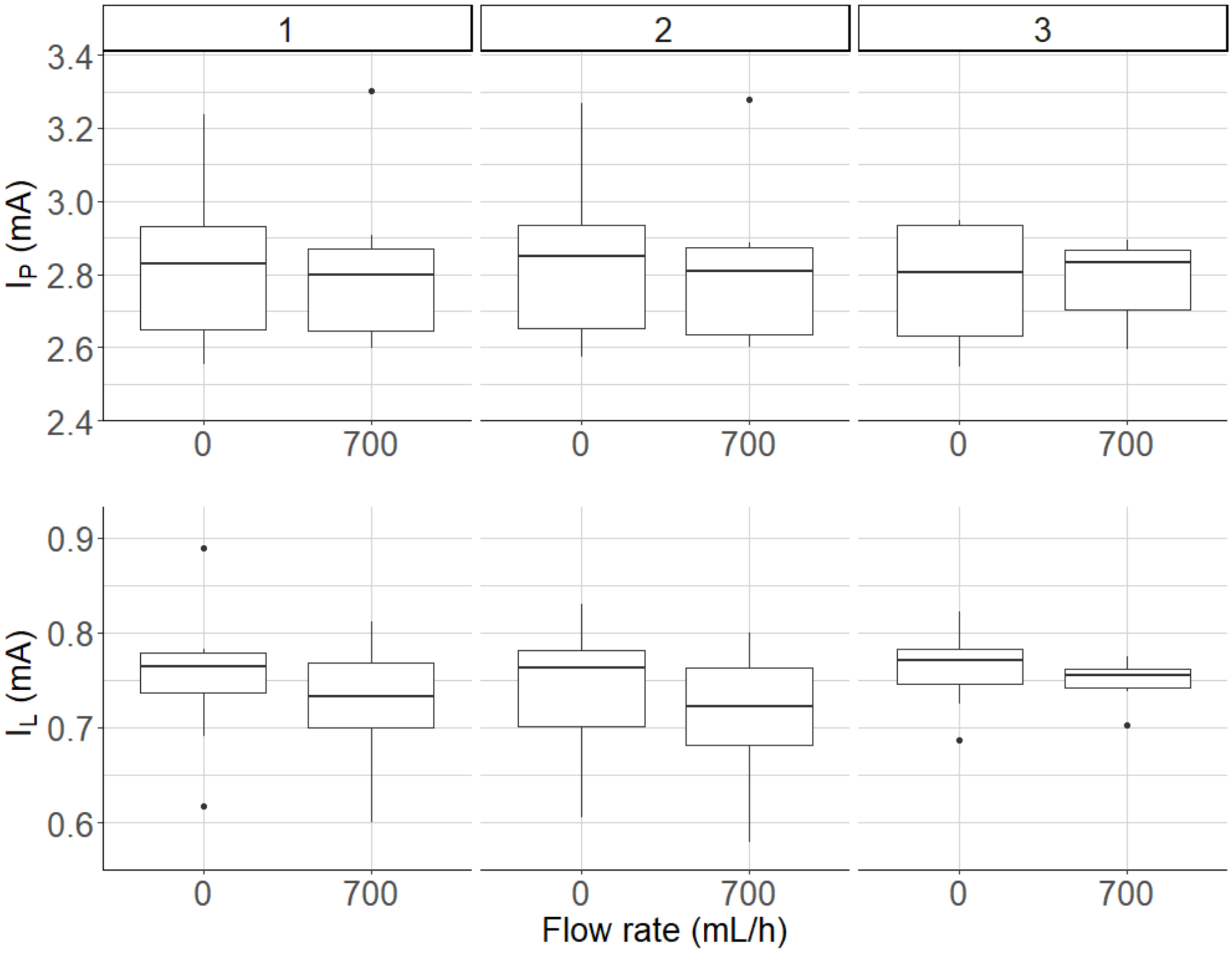

Figure S1: CV cycle and recirculation effect on 8 working electrodes (c-e-h-j-m-o-r-t) acting as anodes oxidizing hexacyanoferrate II, for the values of A) I_P and B) I_L calculated. I_P was considered as the maximum of each anodic curve. I_L is the mean value of the oxidative plateau of the curves from 0.55 to 0.6V/SCE.

Table S1: Correspondence of the R^2 value obtained from the correlation between I_L and hexacyanoferrate (III/II) concentration for the different rotation speeds of the inner cylinder and number of experimental points used for the correlation.

ω (RPM)	0	1	3	5	6.5	8	10	15	25	50	100	150	200
Slope	0.21	0.32	0.47	0.61	0.70	0.71	0.85	1.0	1.5	2.4	3.5	4.2	4.9
Intersect	0.07	0.1	0.2	0.2	0.3	0.5	0.4	0.6	0.4	0.8	1.7	3.8	3.4
R^2	1.00	1.00	1.00	1.00	1.00	0.99	1.00	1.00	1.00	1.00	1.00	0.99	0.99
N	105	195	105	195	105	105	195	90	105	179	180	90	105